

Consequences of long-term water exposure for bulk crystal structure and surface composition/chemistry of nickel-rich layered oxide materials for Li-ion batteries

Henrik L. Andersen,^{a,*} Emily A. Cheung,^a Maxim Avdeev,^{a,b} Helen E. Maynard-Casely,^b Daniel P. Abraham,^c and Neeraj Sharma^a

^aSchool of Chemistry, UNSW Australia, Sydney NSW 2052, Australia

^bAustralian Nuclear Science and Technology Organisation (ANSTO), New Illawarra Road, Lucas Heights, New South Wales 2234, Australia

^cChemical Sciences and Engineering Division, Argonne National Laboratory, Lemont, Illinois 60439, USA

*Corresponding author: Henrik L. Andersen, h.andersen@unsw.edu.au

Keywords: Layered nickel-rich oxides, deuterated water (D₂O) exposure, neutron powder diffraction, Rietveld refinement.

Abstract

Water exposure of layered nickel-rich transition metal oxide electrodes, widely used in high-energy lithium-ion batteries, has detrimental effects on the electrochemical performance, which complicates electrode handling and prevents implementation of environmentally benign aqueous processing procedures. Elucidating the degradation mechanisms in play may help rationally mitigate/circumvent key challenges. Here, the bulk structural consequences of long-term (>2.5 years) deuterated water (D₂O) exposure of intercalation materials with compositions Li_xNi_{0.5}Co_{0.2}Mn_{0.3}O₂ (NCM523) and Li_xNi_{0.8}Co_{0.1}Mn_{0.1}O₂ (NCM811) are studied by neutron powder diffraction (NPD). Detailed inspection of the NPD data reveals gradual formation of a secondary crystalline phase in all exposed samples, not previously reported for this system. This unknown phase forms faster in liquid- compared to vapor-exposed compounds. Structural modelling of the NPD data shows a stable level of Li/Ni anti-site defects and does not indicate any significant changes in lattice parameters or proton-lithium (D⁺/Li⁺) exchange in the structure. Consequently, the secondary phase formation must take place *via* transformation rather than modification of the parent material.

X-ray photoelectron spectroscopy data indicate formation of $\text{LiHCO}_3/\text{Li}_2\text{CO}_3$ at the surface and a Li-deficient oxide in the sub-surface region of the pristine compounds, and the presence of adsorbed water and transition metal hydroxides at the exposed sample surfaces.

1. Introduction

Rechargeable lithium ion batteries (LIBs) remain the energy storage technology of choice for portable electronics, power tools, electric vehicles, *etc.*, owing to their excellent energy and power densities.¹ However, several application limiting factors still exist, which are primarily related to the cathode active materials (CAMs) and their cost, safety, sustainability, rate capability and capacity.^{2, 3} Currently, the layered transition metal oxide family of compounds with the sum formula LiMO_2 , comprising the so-called NCM (M a combination of Ni, Co, Mn) and NCA (M a combination of Ni, Co, Al) materials, constitute the most technologically advanced and commercially successful CAMs.⁴ In particular, the ternary Ni-rich NCM materials, $\text{LiNi}_{x/10}\text{Co}_{y/10}\text{Mn}_{z/10}\text{O}_2$ (NCM $_{xyz}$), where $x+y+z=10$, feature a favorable combination of material cost, chemical/structural stability and electrochemical performance.^{4, 5}

The NCM CAMs crystallize in the layered trigonal structure (space group $R\bar{3}m$) illustrated in Figure 1. The structure consists of alternating layers of octahedrally coordinated Li and Ni/Co/Mn in a cubic close packed (ccp) oxygen lattice. The NCM materials differ from the isostructural LiCoO_2 (first generation material)⁶ by not relying solely on the Co redox couple for the electrochemistry. Instead, the electrochemical reaction and in turn the Li^+ intercalation/extraction is driven by the $\text{Ni}^{2+}/\text{Ni}^{3+}$, $\text{Ni}^{3+}/\text{Ni}^{4+}$ and $\text{Co}^{3+}/\text{Co}^{4+}$ redox couples, with Mn^{4+} generally remaining in the tetravalent state.⁷ The volumetric and gravimetric capacity can effectively be enhanced by increasing the Ni-content, but this generally comes at the cost of lower rate capability and/or reduced safety/stability, which are governed by the Co- and Mn-contents, respectively.^{8, 9} Positive electrodes with NCM523 composition consistently exhibit capacities of approx. 160 mAh/g (depending on voltage/cycling window) while maintaining good structural stability during Li-extraction/insertion.⁴ Increasing the Ni-content further to NCM811 allows reversible capacities exceeding 200 mAh/g to be achieved while maintaining a reasonable cut-off potential (4.2 V vs. graphite).^{5, 10} However, phase-pure NCM materials with high Ni-content are relatively difficult to synthesize. The similar sizes of the Li and Ni ions often lead to cation mixing between the transition metal and Li layers causing formation of the less electrochemically favorable disordered spinel ($Fd\bar{3}m$) and ultimately disordered rock salt ($Fm\bar{3}m$) phases. Although

some Li/Ni anti-site defects are considered beneficial to performance,⁹ the probability of creating spinel phases on surfaces during operation (even without initial Li/Ni mixing) can be detrimental for longer term performance.¹¹ In addition, the Ni-rich NCMs have been shown to be very sensitive to ambient, humid and/or CO₂ containing atmospheres.¹²⁻¹⁴ The higher surface reactivity of Ni-rich materials can lead to formation of a potentially passivating impurity layer on the surface of the CAM particles, which has been shown to have a detrimental effect on the electrochemical properties.¹²⁻¹⁹ Furthermore, the surface reactivity can change the composition of the CAM and thus make it prone to formation of spinel or rock-salt type phases mentioned previously. In this context, the stability of Ni-rich NCM compounds when exposed to H₂O (liquid and vapor) is of particular interest both with the aim of understanding/improving CAM stability in an ambient atmosphere, but also since the applicability of water-based binders/electrolytes,²⁰ aqueous electrode washing procedures,²¹ and hydrothermal synthesis techniques²² are currently being investigated. Consequently, obtaining a detailed understanding of the composition of both bulk and surface impurities and shedding light onto the mechanisms behind their formation are key objectives,⁵ and any insight gained may help facilitate the rational design of improved high-performance NCM cathodes.

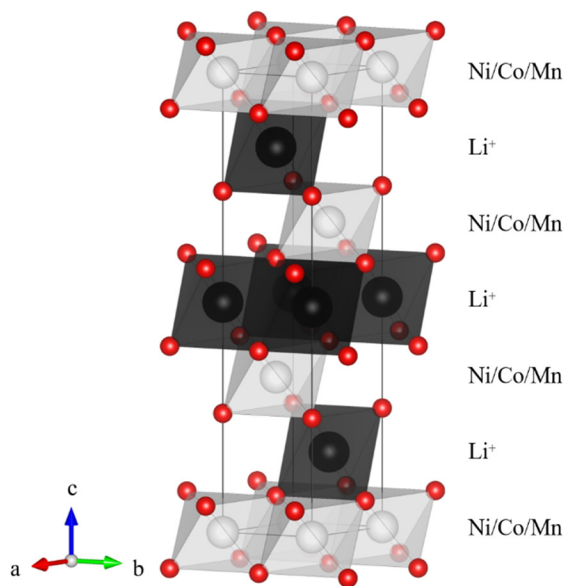
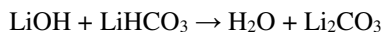
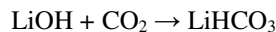
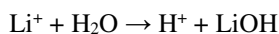


Figure 1: Illustration of the layered LiMO_2 ($M=\text{Ni, Co, Mn}$) structure in the trigonal $R\text{-}3m$ space group (hexagonal setting). The red spheres show the oxygen lattice, while the black spheres/octahedra indicate the positions of Li and the white spheres/octahedra show the positions of the transition metals (*i.e.* Ni, Co, Mn). The illustration has been made using the structure visualization software *VESTA*.²³

In the literature, the exposure of Ni-rich NCM materials to ambient conditions is generally reported to lead to formation of a surface layer consisting of Li_2CO_3 and/or LiOH *via* reactions with ambient CO₂ and H₂O.^{9, 12, 14, 16, 21} Notably, Faenza *et al.*

recently demonstrated how the Li_2CO_3 surface layer formation does not occur by direct reaction with CO_2 alone but requires the presence of moisture to take place. Shkrob *et al.* hypothesized the migration of Li to the surface to be facilitated by a proton-lithium exchange mechanism, *i.e.* outward migration of Li^+ and inward migration of H^+ . These observations suggest LiOH and Li_2CO_3 formation to take place *via* the following reaction pathway:



Furthermore, the induced loss of Li can initiate further reactions such as Li/Ni exchange and provide a Ni rich/Li poor CAM surface that can have implications with further electrochemical cycling. However, the proton-lithium exchange hypothesis is based on inferences from X-ray diffraction (XRD), X-ray photoelectron spectroscopy (XPS), electron microscopy and electrochemical data, *i.e.* no direct/conclusive evidence that protons are inserted into the oxide structure has so far been provided. Similarly, the identification of the Li_2CO_3 /LiOH surface impurity phases in the literature are often based on the observed change in the characteristic oxygen 1s binding energies in XPS data being consistent with a change from the lattice metal-oxide (MO) to CO_3 and/or OH chemistry. However, in a recent paper by Jung *et al.* it was suggested, based on Raman spectroscopy and XPS data (O 1s and Ni 2p photoemission lines) from NCM811 electrodes stored in ambient conditions for 1 year, that formation of a surface layer consisting of NiCO_3 (~10 nm) rather than the commonly assumed Li_2CO_3 and LiOH species likely takes place.¹³ In addition, earlier works on the family of layered materials also show that the surface Ni XPS signal remain after exposure.^{18, 19, 24, 25} Consequently, the nature of the chemistry taking place in and on Ni-rich NCM CAMs when exposed to water and ambient conditions continues to be a subject of interest and debate.

In the present study, the long-term structural stability in two different Ni-rich layered oxide compositions, namely NCM523 and NCM811, exposed to liquid and separately to saturated vapor of deuterated water, D_2O , for a period of >2.5 years, is examined by neutron powder diffraction (NPD). The coherent scattering length of neutrons, b_{coh} , varies between different elements and isotopes and neutron scattering can be used to study a number of light isotopes (including hydrogen (deuterium) and lithium), which are effectively invisible to conventional X-ray diffraction. As a result, NPD data may provide direct evidence of whether D^+/Li^+ exchange, Li/Ni cation mixing and/or Ni/Co/Mn cation ordering takes place as enhanced contrast between these neighboring elements in the periodic table can be obtained.²⁶ Furthermore, NPD is a bulk technique and the high

penetration depth of neutrons allows the entire sample rather than just the surface/near surface to be studied. These attributes make NPD the ideal technique for reliably and representatively determining the composition and structure of NCM CAMs as well as providing direct evidence of any proton-lithium exchange on the condition that enough secondary phase material forms. The presented NPD analysis of the bulk structure is complemented by examination of the outer surface (<10 nm) and sub-surface (at ~50 nm depth by means of ion beam etching) elemental composition and chemistry by X-ray photoelectron spectroscopy (XPS).

2. Experimental

Pristine samples of $\text{Li}_x\text{Ni}_{0.5}\text{Co}_{0.2}\text{Mn}_{0.3}\text{O}_2$ (NCM523) and $\text{Li}_x\text{Ni}_{0.8}\text{Co}_{0.1}\text{Mn}_{0.1}\text{O}_2$ (NCM811) were supplied by Argonne's Cell Analysis, Modeling and Prototyping (CAMP) Facility. The samples were divided in three parts as follows: I) The first part (control sample) was stored in an inert atmosphere in an Argon filled glovebox. II) The second part was exposed to D_2O vapor (100% humidity) in a closed Schott flask. III) The third part was immersed in deuterated water and stored in a closed Al can. The samples were stored at room temperature (constantly regulated by air conditioning).

The NPD data collection were carried out using the high-resolution powder diffractometer ECHIDNA^{27, 28} at the OPAL research reactor, Australian Nuclear Science and Technology Organisation (ANSTO), at room temperature using a wavelength of 1.6215 Å. Data for the pristine samples were collected from powder filled in 9 mm vanadium cans while the exposed sample data were collected from powders in custom-built sealed aluminium containers, which were also used to store the samples. Over the course of >2.5 years, NPD patterns of NCM523 and NCM811 samples exposed to D_2O vapor and liquid were regularly collected, *i.e.* after 0, 9, 18, 34, 43, 61 and 135 weeks. In addition, NPD data on the NCM523 and NCM811 control samples (stored in inert atmosphere) were collected after 0, 36 and 135 weeks. The same instrumental configuration and data collection time were used for every pattern. Simulations and Rietveld refinements of structural models to the NPD patterns were carried out using the *FullProf Suite* software package.²⁹

The XPS spectra were collected under ultrahigh vacuum ($<2 \cdot 10^{-9}$ mbar) conditions on a Thermo ScientificTM ESCALABTM 250Xi⁺ spectrometer equipped with a monochromatic Al K α (1486.68 eV) X-ray source. The spectrometer was calibrated from characteristic Au 4f7 (83.96 eV), Ag 3d5 (368.21 eV) and Cu 2p3 (932.62 eV) binding energy peaks from reference specimens. Spectra were collected from the pristine and D_2O liquid exposed (>2.5 years) NCM523 and NCM811 samples, both from the as-received surfaces as well as after 300s of ion beam etching to a depth of approximately 50 nm. Note that the samples were briefly exposed to air during sample loading into the XPS chamber. The obtained spectra were processed and analysed using

the Thermo Scientific™ *Avantage Data System*. For each spectrum, the binding energies were calibrated from the adventitious hydrocarbon C 1s peak position (284.8 eV) and peak fitting was carried out by Gaussian-Lorentzian curve synthesis using a Shirley background correction.

3. Results and Discussion

The Results and Discussion section is divided into three parts. In the first part, the structure of the unexposed pristine NCM523 and NCM811 samples are determined by Rietveld analysis of NPD data thereby establishing the foundation for the study by providing a reference point for any observed structural changes. The second part concerns the bulk structural consequences of D₂O exposure and investigates the exposure-induced formation of a secondary crystalline phase and the evolution in key structural parameters (*e.g.* cell parameters, anti-site defects and D⁺/Li⁺ exchange) as function of exposure type (D₂O vapor or liquid) and time. In the third part, the influence of the D₂O liquid exposure on the surface and sub-surface elemental composition and chemistry of the samples is examined by XPS.

3.1. Crystal structure - Pristine samples

Figure 2 shows the NPD data and Rietveld-refined fits of the pristine NCM523 and NCM811 samples. The refinements were based on the layered trigonal structure (space group *R-3m*). Summaries of the employed atomic models and refined structural parameters for the pristine NCM523 and NCM811 samples are provided in Table 1 and Table 2, respectively. The occupations of Co and Mn on the 3*a* transition metal site as well as O on the 6*c* site were fixed based on the nominal compositions of the samples. The Li and Ni occupancies on the 3*b* and 3*a* sites were refined with a constraint to the nominal composition. Common isotropic atomic displacement parameters (B_{iso}) were refined for each crystallographic site. An absorption correction was implemented in the refinements based on an estimated linear attenuation factor, diameter and packing density of the samples. The instrumental contributions to the total peak broadening and peak asymmetry were determined by measuring NPD data of NIST LaB₆ 660b standard under the same instrumental configuration followed by Rietveld analysis. The resulting instrumental resolution function was implemented in the refinements to deconvolute the sample and instrumental line profiles. The sample peak profiles were fitted using the Thompson-Cox-Hastings formulation of the pseudo-Voigt function³⁰ employing one Gaussian profile parameter related to microstrain. The sample displacement parallel and perpendicular to the beam direction was refined and the background was described by a 12 coefficient Chebychev polynomial.

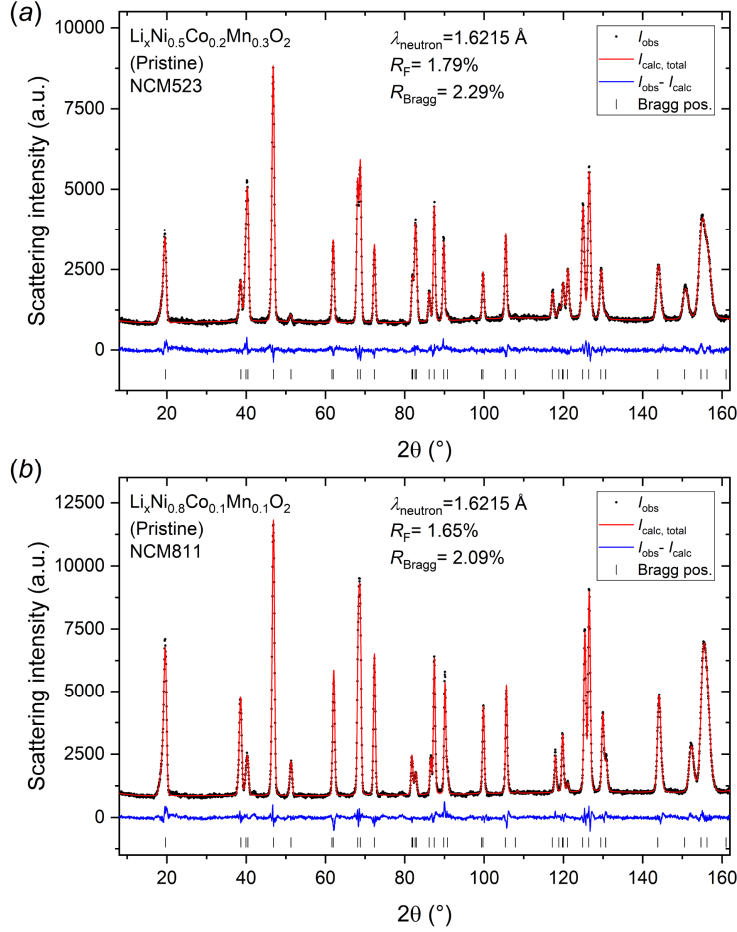


Figure 2: High-resolution neutron powder diffraction data (black) and corresponding Rietveld refined structural model (red) of (a) pristine NCM523 and (b) pristine NCM811 samples. The error bars of the NPD data points are smaller than the symbols.

The employed model yielded a good match for both the pristine NCM523 and NCM811 samples ($R_F = 1.79\%$ and $R_F = 1.65\%$, respectively), confirming the samples to be phase-pure and of the expected stoichiometry. The refinements did not suggest any cation ordering to be present in the pristine samples as evident from the good description of the relative peak intensities. The pristine NCM523 sample exhibited a minor amount of Li/Ni anti-site defects of 4.2(1)%, while the refinements did not suggest any Li/Ni cation site mixing to be present in the NCM811 sample. This observation is in good agreement with previously reported anti-site defect concentrations for the studied compositions.^{26, 31}

Table 1: Crystallographic parameters for the pristine NCM523.

NCM523 (Li _x Ni _{0.5} Co _{0.2} Mn _{0.3} O ₂) - pristine						
Space group: $R\bar{3}m$ (No. 166)						
$a=b=2.87098(2)$ Å, $c=14.2506(1)$ Å, $\alpha=\beta=90^\circ$, $\gamma=120^\circ$						
$R_{\text{Bragg}}=2.29$ %, $R_{\text{F}}=1.79$ %						
Atom	Site	x	y	z	B_{iso} (Å ²)	Sof^a
Li	3b	0	0	0.5	2.05(6) ^b	0.958(1) ^d
Ni	3b	0	0	0.5	2.05(6) ^b	0.042(1) ^d
Li	3a	0	0	0	1.21(2) ^c	0.042(1) ^d
Ni	3a	0	0	0	1.21(2) ^c	0.458(1) ^d
Co	3a	0	0	0	1.21(2) ^c	0.2
Mn	3a	0	0	0	1.21(2) ^c	0.3
O	6c	0	0	0.25844(4)	1.68(1)	1

Note: The numbers in parentheses indicate the errors on the last significant digit of the refined parameters.

^aSite occupation fraction. ^{b,c}The atomic displacement parameters (B_{iso}) of atoms on the same sites were constrained to be equal. ^dConstrained to nominal composition.

Table 2: Crystallographic parameters for the pristine NCM811.

NCM811 ($\text{Li}_x\text{Ni}_{0.8}\text{Co}_{0.1}\text{Mn}_{0.1}\text{O}_2$) - pristine						
Space group: $R\bar{3}m$ (No. 166)						
$a=b=2.87154(1)$ Å, $c=14.1978(1)$ Å, $\alpha=\beta=90^\circ$, $\gamma=120^\circ$						
$R_{\text{Bragg}}=2.09\%$, $R_{\text{F}}=1.65\%$						
Atom	Site	x	y	z	B_{iso} (Å ²)	Sof^a
Li	3b	0	0	0.5	2.75(6) ^b	1.001(1) ^d
Ni	3b	0	0	0.5	2.75(6) ^b	-0.001(1) ^d
Li	3a	0	0	0	1.12(1) ^c	-0.001(1) ^d
Ni	3a	0	0	0	1.12(1) ^c	0.8001(1) ^d
Co	3a	0	0	0	1.12(1) ^c	0.1
Mn	3a	0	0	0	1.12(1) ^c	0.1
O	6c	0	0	0.25878(5)	1.71(1)	1

Note: The numbers in parentheses indicate the errors on the last significant digit of the refined parameters.

^aSite occupation fraction. ^{b,c}The atomic displacement parameters (B_{iso}) of atoms on the same sites were constrained to be equal. ^dConstrained to nominal composition.

3.2. Structural stability/evolution - D_2O exposed samples

As discussed in the introduction, Shkrob *et al.* recently hypothesized a proton-lithium exchange mechanism to be the driving force behind the extraction of Li^+ and, in turn, the formation of the Li_2CO_3 surface layer in weathered NCM523 electrodes.¹² In the present study, NPD data were collected regularly over a period of >2.5 years (135 weeks) on NCM523 and NCM811 powders exposed to deuterated water (saturated vapor and liquid). The common hydrogen isotope, ^1H , (99.985% of naturally occurring hydrogen) has a very high incoherent neutron scattering length, b_{inc} , (25.274 fm) giving rise to a large background signal in neutron scattering data.³² However, the deuterium isotope, ^2D , has a relatively high b_{coh} (6.671 fm) as well as a low b_{inc} (4.04 fm).³² In combination with the very high contrast between D and Li ($b_{\text{coh}} = -1.90$ fm), using D_2O instead of H_2O allows us to directly probe whether deuterons replace the lithium ions in the structure given that a significant amount of proton-lithium exchange occurs. Furthermore, the high penetration depth of neutrons allows the true bulk structure to be examined and real representative quantities (gram scale) of materials to be characterized.

3.2.1. Secondary crystalline exposure product phase

Figure 3 shows selected regions of the NPD patterns collected on NCM523 and NCM811 pristine samples stored in an inert atmosphere for 0, 36 and 135 weeks and samples exposed to D₂O vapor and liquid for 0, 61 and 135 weeks. The refinement of the NPD data from the samples were based on the structural model described earlier for the pristine samples. For the exposed samples, a metallic aluminium phase (space group *Fm-3m*) was added to account for the contribution from the employed Al sample holder (approximately 15-20 wt%). The full NPD patterns and Rietveld fits for all exposure times may be found in the Supporting Information. The NPD patterns of the pristine NCM523 and NCM811 samples stored under inert conditions show no signs of degradation or formation of additional phases (see Figure 3 a) and d)). However, the exposure of NCM523 and NCM811 to D₂O vapor is found to cause formation of a secondary crystalline phase, as evident from the weak peak appearing at a 2θ -value of approximately 37.3° (see arrows in Figure 3 b) and e)). For the samples exposed to liquid D₂O, gradual appearance of the same reflection along with three additional peaks likely arising from the same secondary phase is readily observed as indicated by the arrows in Figure 3 c) and f)). Thus, the increased contact between D₂O and CAM during exposure to liquid water seems to accelerate the secondary phase formation. Notably, the datasets collected on the same compounds stored under inert conditions show no signs of any crystalline impurities forming (see Supporting Information).

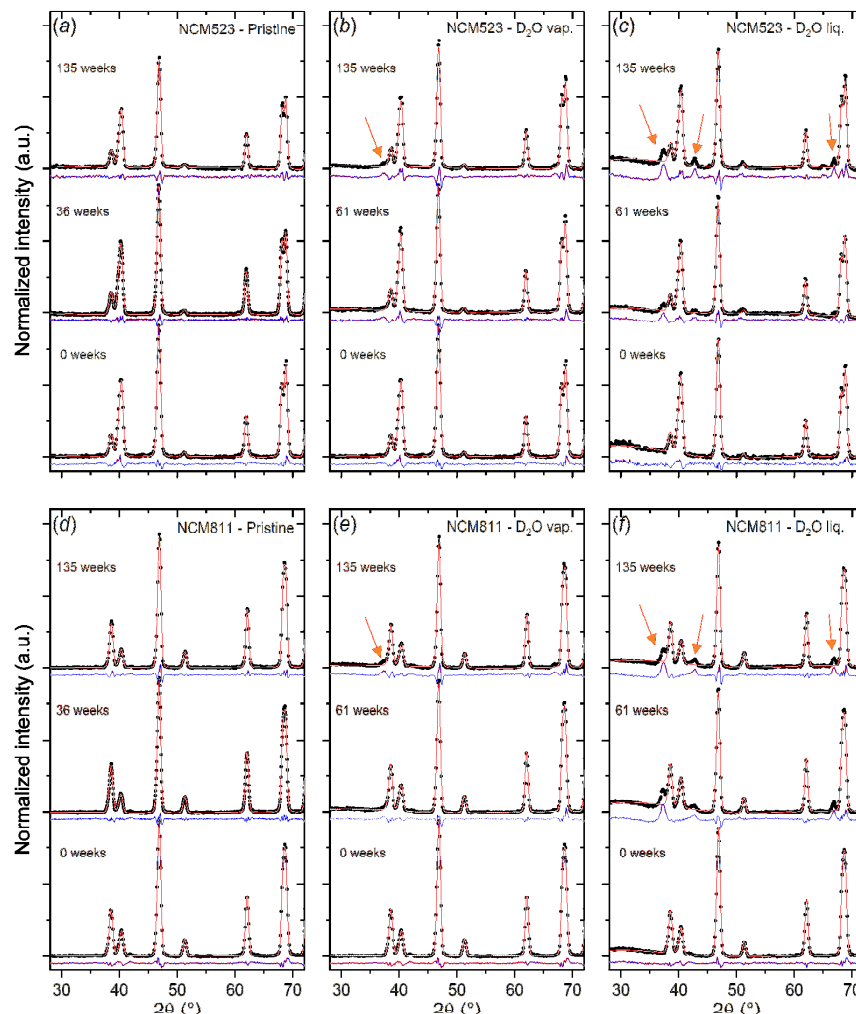


Figure 3: Selected regions in the NPD data (black), Rietveld refined line profiles (red) and difference curves (blue) for a) NCM523 pristine, b) NCM523 exposed to D₂O vapor, c) NCM523 exposed to D₂O liquid, d) NCM811 pristine, e) NCM811 exposed to D₂O vapor, and f) NCM811 exposed to D₂O liquid, stored for the indicated times. The error bars on the NPD data points are smaller than the symbols. The arrows indicate the positions of additional peaks appearing in the NPD patterns of the NCM523 and NCM811 liquid D₂O exposed samples. The NPD data were collected with a wavelength of 1.6215 Å. The full NPD datasets and Rietveld fits (*i.e.* entire 2 θ -ranges) as well as datasets obtained after additional exposure times may be found in the Supporting Information.

In the literature, the appearance of reflections from Li₂CO₃ in space group *C12/c1* in powder diffraction data is often reported when storing similar compounds under ambient or humid conditions.^{15, 24, 33} However, the reflections observed here do not correspond to the characteristic peak positions of the Li₂CO₃ phase as illustrated in Figure 4b. Attempts at assigning the peaks to other usual suspect structures, *i.e.* LiOH, NiCO₃, the spinel (LiNi₂O₄) and rock-salt (NiO) phases were also unsuccessful (see Figure 4c-f). Running a database search based on the observed secondary phase's d-spacings in the

*HighScore+*³⁴ software did not yield any plausible candidates. Synthetic NPD patterns of many additional candidate structures were manually compared to the data (see Supporting Information) but no plausible matches were found. The candidate coming closest to matching the peak positions and relative intensities is the manganese oxyhydroxide MnO(OH) in space group *Pnma* (see Supporting Information), however, assigning this phase based on the rough indexation alone would not be justifiable and the identity of the secondary phase thus remains unknown. An *ab initio* determination of the unit cell and space group of the secondary phase (based on the four reflections at 2θ -values 37.30°, 42.75°, 66.87° and 79.10°) was carried out using the structure solution software *EXPO2014*.³⁵ A tetragonal structure in space group *P4/mmm* with lattice parameters $a=b=2.3260$ Å, $c=7.6076$ Å was proposed, however, such small *a*- and *b*- cell parameters are not plausible for any oxide. Undertaking a full structure solution from these NPD data was not deemed feasible given the data quality, *i.e.* the low intensity of the secondary phase peaks, and its unknown elemental composition. The fact that the new phase formed in the powders immersed in liquid water in combination with the appearance of a peak with rather large d-spacing (~ 7.6 Å) could suggest the possibility of water intercalation into the interlayer space or formation of another hydrate phase. The observation of this secondary crystalline phase is completely different compared to previous studies of water exposed NCM CAMs, which are limited by the techniques that are employed and predominantly characterize the outer surface of the materials. In the present study, the use of neutron diffraction has enabled us to elucidate the truly bulk-level structural evolution and discover the formation of the secondary phase as a result of D₂O exposure.

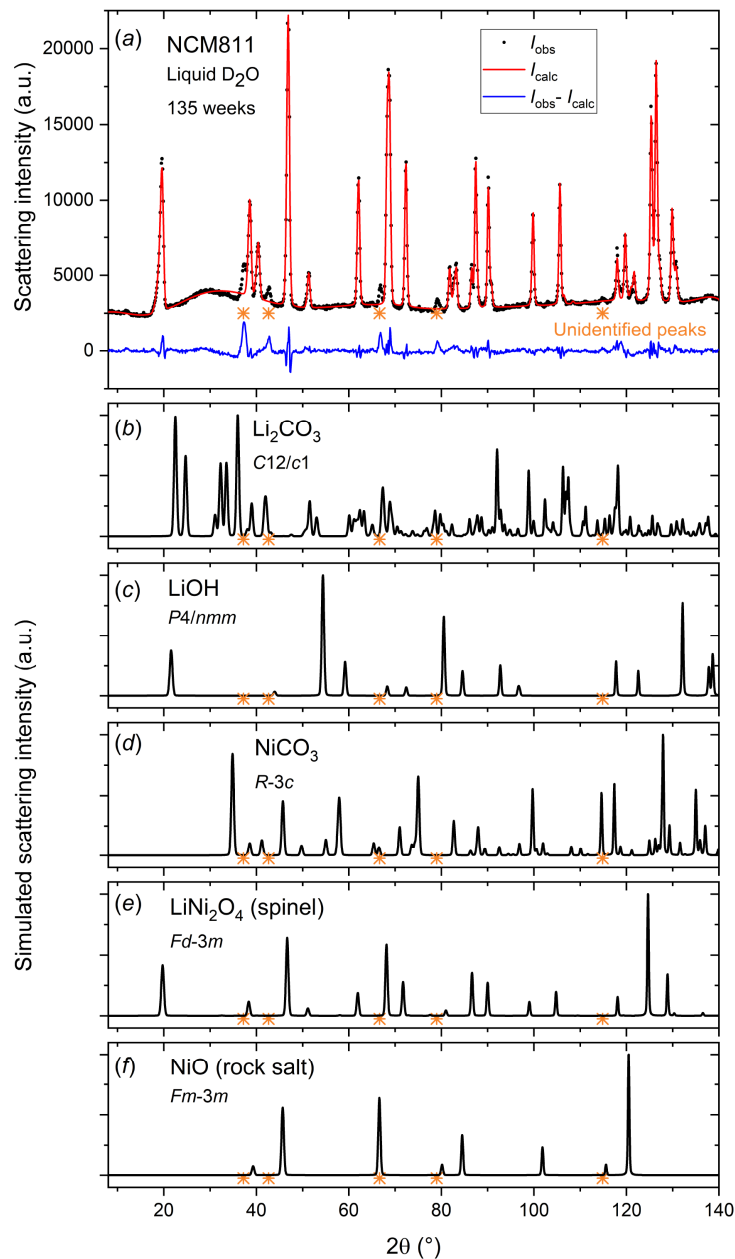


Figure 4: a) NPD data and Rietveld refined line profile for the NCM811 data exposed to liquid D₂O for 135 weeks. The positions of unidentified peaks are indicated by orange asterisks. The error bars on the NPD data points are smaller than the symbols. Positions of unidentified peaks (orange asterisks) relative to simulated NPD patterns of commonly reported secondary phases; b) Li₂CO₃,³⁶ c) LiOH (deuterated),³⁷ d) NiCO₃,³⁸ e) LiNi₂O₄ spinel phase,³⁹ and f) delithiated rock-salt phase NiO.⁴⁰

3.2.2. *Secondary phase – formation rate*

Figure 5a-d shows the gradual increase in intensity of the primary reflection from the unknown secondary phase, here plotted as the difference curve from the background subtracted and normalized Rietveld fit. The rate of the phase formation may be evaluated based on the evolution in peak area (extracted by fitting a simple Gaussian peak) due to its direct correlation with the probed material volume. As seen in Figure 5e-f, the secondary phase formation is clearly more pronounced in the liquid D₂O exposed samples for both NCM523 and NCM811. Furthermore, the secondary phase formation progresses faster in the liquid D₂O exposed NCM811, which is consistent with the Ni-rich NCM compounds being less stable. Notably, the formation of the secondary phase in the NCM811 sample seemingly stalls after 61 weeks as no additional secondary phase has formed after 135 weeks, while it continues to develop in the NCM523 sample. As a result, after 135 weeks similar amounts of secondary phase are observed in the NCM523 and NCM811 liquid exposed samples. However, considering the uncertainties of the data points, no reliable kinetic growth model or phase formation rate can be extracted.

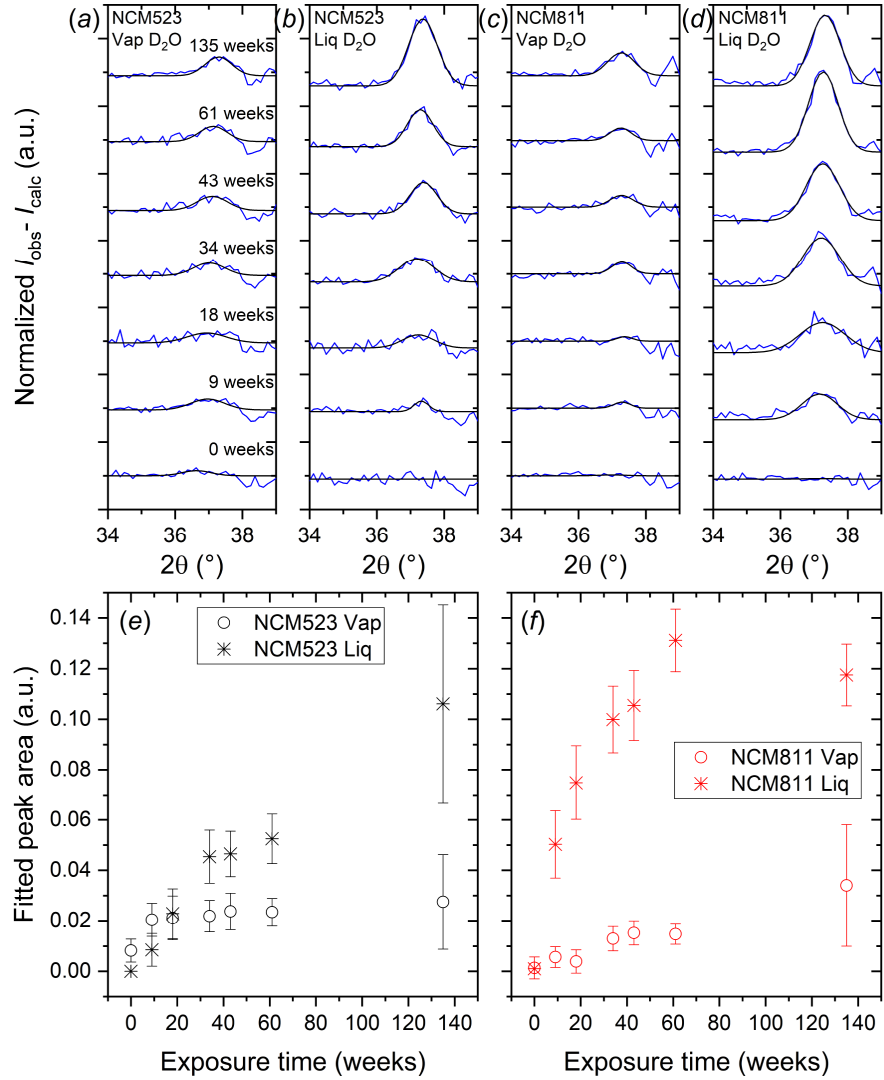


Figure 5: Normalized difference curves (blue) from the Rietveld refinements in a selected 2θ-region illustrating the formation unidentified secondary phase in a) NCM523 exposed to D₂O vapor, b) NCM523 exposed to D₂O liquid, c) NCM811 exposed to D₂O vapor and d) NCM811 exposed to D₂O liquid. The curves have been fitted by a Gaussian profile (black). e) Fitted peak area as function of exposure time for the NCM523 samples. f) Fitted peak area as function of exposure time for the NCM811 samples.

3.2.3. Evolution in lattice parameters

For layered oxides, the chemical or electrochemical extraction of Li⁺ ions (up to a certain point)^{33, 41, 42} is generally associated with an expansion of the structure along the crystallographic c-axis and contraction along the a/b-axes due to increased interlayer oxygen-oxygen repulsion and oxidation of the transition metals, respectively.⁹ Hydration, *i.e.* intercalation of water molecules between the structural layers, would also give rise to an expansion along the c-axis, however, this effect is much

more pronounced.⁴³ Interestingly, the study by Shkrob *et al.* showed that 2 months exposure of NCM523 electrodes caused minor contraction (-0.056%) along the c-axis and expansion (0.026%) in the ab-plane.¹² This observation, along with XPS data (O 1s binding energy changes) suggesting formation of a $\text{CO}_3^{2-}/\text{OH}^-$ species at the surface, led them to propose a proton-lithium exchange driven formation of a $\text{Li}_2\text{CO}_3/\text{LiOH}$ surface layer during exposure of NCM to high-humidity environments, with the competition between the lithium extraction (c-axis expansion/a-axis contraction) and proton intercalation (c-axis contraction/a-axis expansion) processes explaining the minor/negligible changes in the lattice parameters.

Figure 6 shows the evolution in lattice parameters as function of exposure time for the NCM523 and NCM811 samples in the present study. For both compositions, a significant a-axis expansion and c-axis contraction occurs when subjecting the pristine samples to liquid D_2O even for a short time (data points at 0 weeks exposure time) and D_2O vapor for 9 weeks. However, following these initial changes the lattice parameters remain largely constant showing no additional systematic or significant variations. Notably, the formation of the secondary phase discussed above does therefore not seem to affect the lattice parameters of the NCM parent phases. Removing a single type of metal by leaching would lead to changes in lattice parameter due to the different atomic radii of the metal ions and would furthermore give rise to charge compensation issues. This observation could therefore imply that the secondary phase is formed by the transformation of the parent phase rather than its modification. Note for the 135 weeks pristine sample, slight exposure to non-inert conditions occurred due to glovebox relocations.

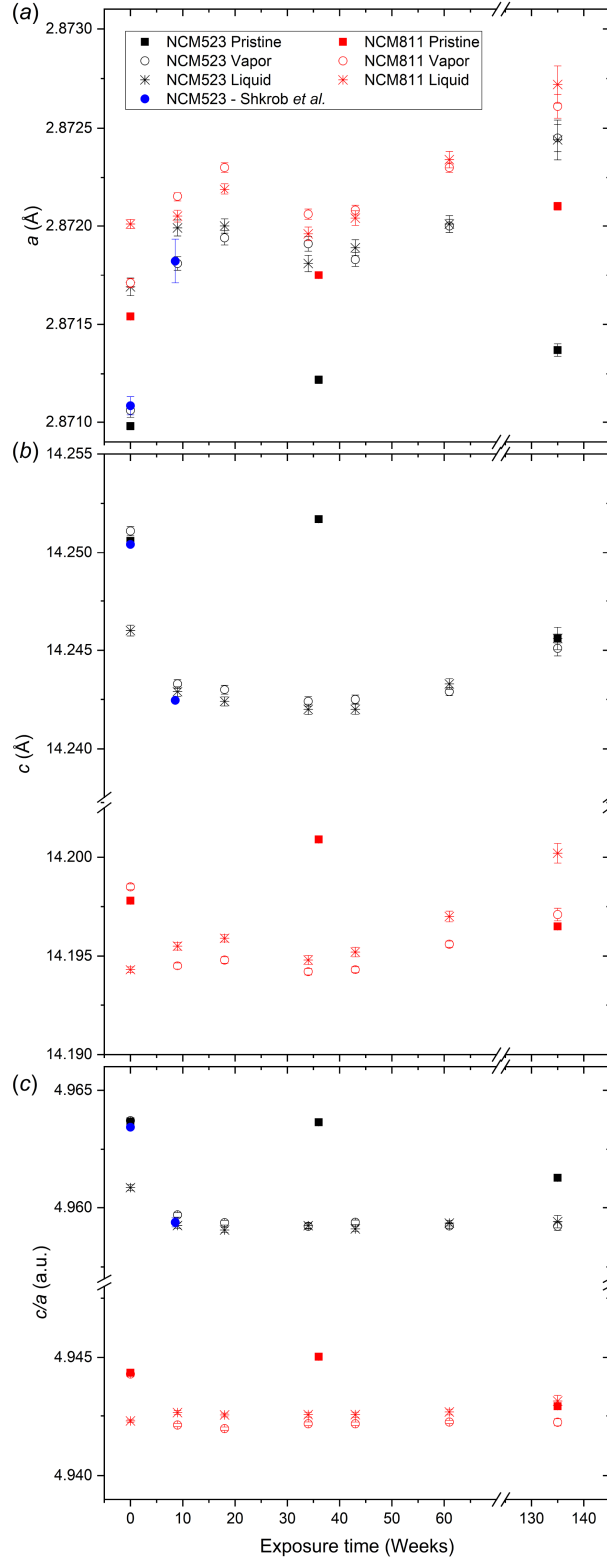


Figure 6: Refined lattice parameters (a) a , (b) c and (c) c/a as function of exposure time for the indicated samples.

3.2.4. Li/Ni anti-site defects and D^+/Li^+ exchange

The differences in coherent neutron scattering lengths, b_{coh} , between ^2D ($b_{\text{coh}}=6.671(4)$ fm), Li ($b_{\text{coh}}=-1.90(2)$ fm), and Ni ($b_{\text{coh}}=10.3(1)$ fm),³² are expected to provide sufficient contrast to observe if deuteron-lithium exchange and/or Li/Ni cation mixing occurs. Taking the pristine NCM523 NPD data as an example (initially without considering D^+/Li^+ exchange), various structural models and refinement approaches were trialed, including free occupancy refinement and introduction of vacancies. However, these models yielded either unphysical site populations or poorer fit statistics compared to the employed model which was constrained to the nominal composition. The values of Li/Ni site mixing, calculated from the refined site occupation fractions, as function of exposure time in the different sample series are shown in Figure 7. The Li/Ni site mixing in the NCM523 (~4%) and NCM811 (0%) remain seemingly unaffected by both D_2O vapor and liquid exposure. The very small errors seen in the figure indicate that the refined site occupation fractions are relatively robust and that even small changes in site population would therefore be detectable given the scattering contrast between the constituent elements.

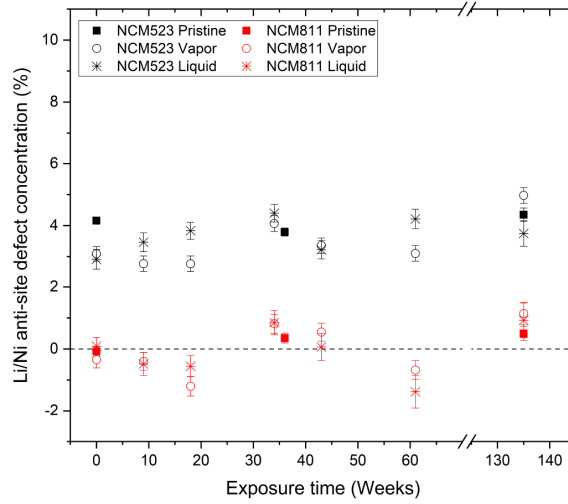


Figure 7: Refined Li/Ni site mixing (*i.e.* percentage of Li on the transition metal site) as function of exposure time for the indicated samples.

In order to test for deuteron-lithium exchange, two different models were tested both on the pristine NCM523 and NCM811 NPD data as well as liquid D_2O exposed NCM523 and NCM811 NPD data. Model 1 allowed direct exchange of D^+ for Li^+ into the $3b$ site. In model 2, the D^+ was placed pointing into the Li-layer at a distance of 1 Å (approximate D-O covalent bond length) from the oxygen. In both models, the Li/Ni anti-site defect concentration was fixed to the values obtained for the pristine samples while the refinement of the occupancies was controlled by implementing appropriate linear restraints on the D^+/Li^+ substitution. The obtained D^+/Li^+ exchange percentages as function of exposure time are plotted in Figure 8.

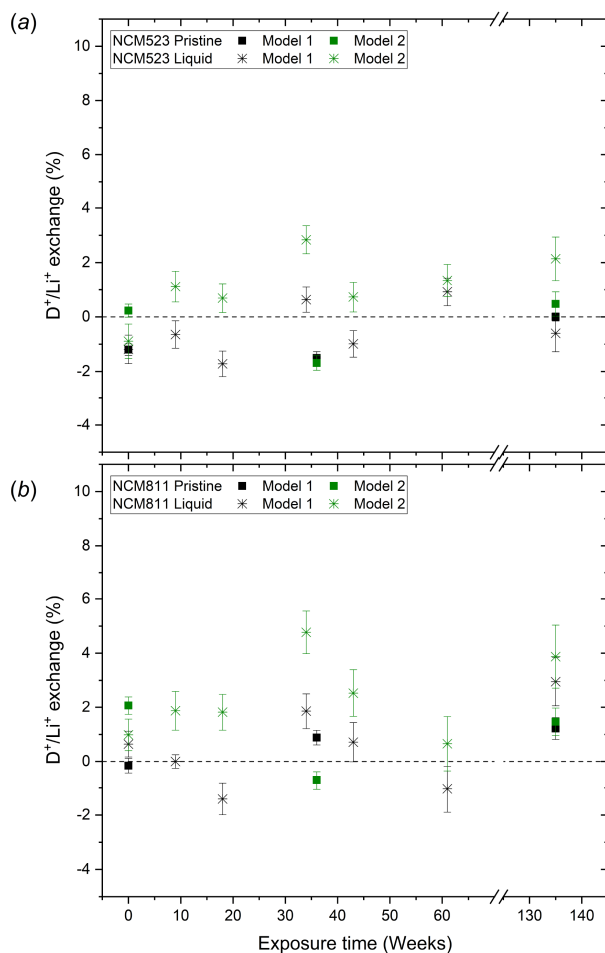


Figure 8: Refined deuteron-lithium exchange percentage as function of exposure time for a) NCM523 pristine and liquid D_2O exposed, and b) NCM811 pristine and liquid D_2O exposed.

Considerable fluctuations are observed in the refined D^+/Li^+ exchange percentages, and no trends can be reliably discerned with respect to composition, model, exposure type, or time. The lack of statistically significant changes in cell parameters (Figure 6) and refined D^+/Li^+ exchange percentages (Figure 8) indicates that little to no proton-lithium exchange occurs in NCM523 or NCM811 under the studied conditions. Although the errors and variance between data points in the series are too large to confidently conclude notable amounts of D^+/Li^+ exchange, it should be noted that in some instances D^+/Li^+ exchange percentages as high as ~5% are obtained, which is comparable to the level of proton/lithium exchange (5-8%) suggested by Shkrob *et al.*¹² As discussed above, the degradation of both materials is observed *via* the formation of a secondary phase (Figure 5). Consequently, it is strongly suggested that the secondary phase is formed by the transformation of the parent phase rather than its modification.

3.3. Surface composition and chemistry

The exposure of NCM CAMs to humid conditions is known to adversely affect their electrochemical performance.^{12, 15, 16, 19, 44} This is generally attributed to formation of an inactive/passivating surface layer, however, the influence of the previously unreported bulk crystalline secondary phase observed by NPD here has yet to be determined. Several studies report Li_2CO_3 and/or LiOH to be the main surface species forming in NCM materials after exposure to air or humid conditions.^{15, 17, 44-48} However, the nature of the surface impurities and the mechanisms behind their formation are a subject of continued discussion in the literature. Liu *et al.* proposed that the spontaneous reduction of Ni^{3+} at the surface of LiNiO_2 powders triggers the formation of active oxygen species, which can react with Li and ambient H_2O and CO_2 to form LiOH , LiHCO_3 and Li_2CO_3 .²⁴ Shkrob *et al.* suggested that the delithiation associated with the formation of the Li-containing surface species could be coupled with H^+/Li^+ cation exchange in the NCM structure.¹² Faenza *et al.* suggested a three-step reaction mechanism, where Li_2CO_3 is formed via LiOH and LiHCO_3 intermediates, rather than by direct reaction of Li with ambient CO_2 .¹⁶ Notably, a recent study by Jung *et al.* argued that formation of a surface layer consisting of NiCO_3 (~10 nm) rather than the commonly reported Li_2CO_3 and LiOH species likely takes place.¹³ This conclusion was in part based on the Ni 2p photoelectron emission line remaining visible in the XPS data from the surface after water exposure despite the O 1s metal oxide feature completely disappearing. Several earlier works on the NCM family of layered materials also show that the surface Ni XPS signal remain after exposure.^{18, 19, 24, 25} Some reports indicate that the observation of Li-containing surface species may be attributed to unreacted residual precursor from the synthesis.^{18, 49, 50} Furthermore, many of the previous studies have been conducted on full electrode mixtures containing different amounts of conductive carbon, PVDF binder, *etc.*, which have been exposed to various types of electrolyte and electrochemical cycling. This introduces several additional components which must be considered when comparing studies.

3.3.1. XPS - Spectral features

XPS is a highly surface-sensitive quantitative spectroscopic technique which provides information about the elemental composition, as well as the distinct element specific chemical environments and electronic states of elements in the outermost atomic layers (<10 nm) of a material.^{51, 52} In the present study, XPS data have been collected for the pristine NCM523 and NCM811 powders and their D_2O liquid exposed equivalents in order to investigate the consequences of long-term water exposure on the surface composition and chemistry of the cathode active material. Spectra were collected from the as-prepared surfaces as well as after 300s of ion beam etching to a depth of approximately 50 nm to examine and compare the composition and chemical nature of the surface layer to that of the sub-surface material. Note that the XPS data was collected on powders,

and the ion beam etching will therefore not directly reveal the true bulk composition/chemistry as some degree of the outer surface will inherently still be probed. Furthermore, the process of etching itself may alter the oxidation state and chemical nature of the probed surface. Full range survey scans (see Supporting Information) were initially performed for each sample to identify all elements present, followed by higher resolution scans in specific regions around the characteristic core electron binding energies (BEs) of the identified constituent elements, *i.e.* Li 1s, Ni 2p, Co 2p, Mn 2p, O 1s, of the NCM materials as well as C 1s. The obtained spectra are shown in in Figure 9 for NCM523 (pristine and D₂O liquid exposed) and in Figure 10 for NCM811 (pristine and D₂O liquid exposed).

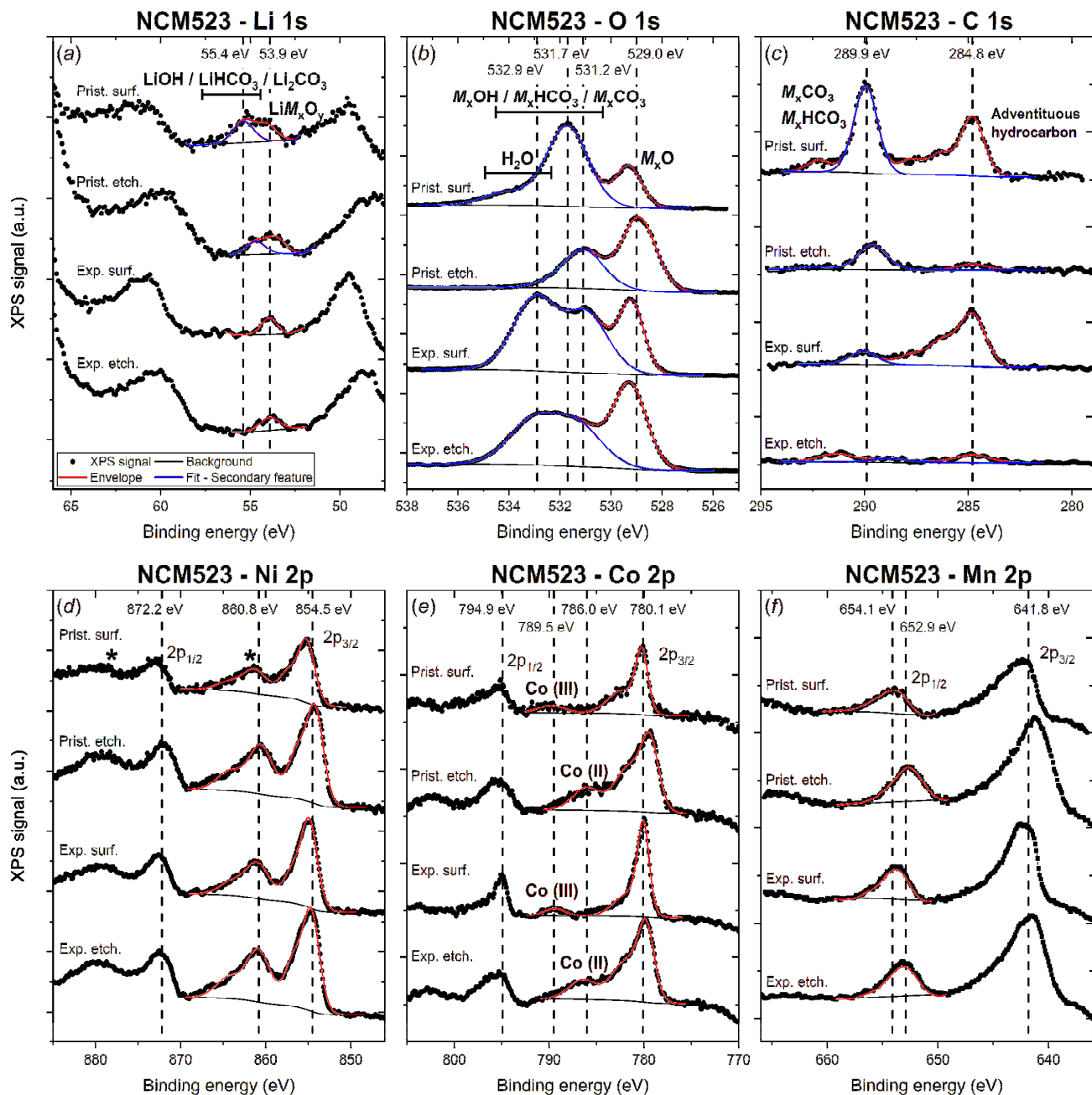


Figure 9: Stacked plots of background normalized XPS spectra of the a) Li 1s region, b) O 1s region, c) C 1s region, d) Ni 2p region, e) Co 2p region, and f) Mn 2p region of the pristine and D₂O liquid exposed (>2.5 years) NCM523 sample. For each sample spectra were collected from the as-received surface and after 300 s of ion beam etching to approximately 50 nm depth.

For the pristine NCM523 and NCM811, the Li 1s spectra (both surface and etched) clearly exhibit two features, which are consistent with previously reported intercalated structural Li in the NCM material (~53.9 eV) and Li in an additional phase (~55.4 eV), *e.g.* LiOH, LiHCO₃ or Li₂CO₃.^{21, 53} Interestingly, the spectra (surface and sub-surface) of the exposed NCM523 sample only show the lower BE feature at (~53.9 eV) from the NCM oxide indicating no Li-containing hydroxide or carbonate

additional phases to be present. Similarly, the exposed NCM811 sample shows a smaller amount of Li-containing additional phases at the surface and none after etching.

For all samples, the O 1s XPS spectrum comprises a low BE feature (~529 eV) and several overlapped peaks at higher BE (~530-534 eV). The distinct low BE peak corresponds to lattice oxygen in a metal oxide,⁵¹ which here is likely to be the NCM material, but could potentially come from spinel and/or rock-salt metal oxide phases previously reported for the system.¹² The number of possible oxygen chemistries in the higher 530-534 eV BE-range is very large,⁵¹ and the substantial overlap of the observed features makes them difficult to reliably discern. As a result, deconvoluting the peaks and assigning the contributions from the various chemical environments is not a straightforward task. Given the context of the present system, the peaks most likely arise from one or more metal hydroxide (M_xOH), bicarbonate (M_xHCO_3) and/or carbonate (M_xCO_3) species along with some degree of adventitious oxygen-containing surface contamination species, such as organic oxygen and/or water. Notably, the surface XPS spectra of pure transition metal oxide sample, including the compositions studied here, are known to exhibit a second higher BE peak in the ~530-532 eV region.^{54, 55} This feature can be attributed to a defective oxide component (and not hydroxide/carbonate species) inherently forming at the surface,^{56, 57} and it is known to contribute up to 20-40% of the total O 1s peak intensity from the given transition metal oxide.⁵⁷⁻⁵⁹

For the pristine and D₂O exposed surfaces of the NCM523 sample, a clear difference is observed in the line shapes in the overlapped high BE region revealing differences in the secondary surface phases present. Apart from the characteristic metal oxide feature at ~529 eV, the pristine NCM523 O 1s surface spectrum exhibits one dominant feature in the higher BE region with a maximum at ~531.7 eV, which likely contains several minor contributions, *e.g.* in the tail seen towards higher BE. On the other hand, the D₂O exposed NCM523 surface spectrum contains two major features in the high BE-range with maxima at ~531.2 eV and ~532.9 eV, respectively. The O 1s line of metal-carbonates typically has a lower binding energy than corresponding metal-hydroxides and this could thus indicate co-existence of the two,⁵¹ but reported values of their specific BEs vary substantially.^{12, 13, 19, 53} Like NCM523, the pristine NCM811 surface O 1s spectrum also exhibits the characteristic metal oxide feature at lower BE (~529 eV) along with one dominant feature at higher BE (~531.7 eV) from secondary oxygen species. However, the O 1s line shape in the 530-534 eV BE-range of the exposed NCM811 spectrum is substantially different from the NCM523 sample. Like the pristine sample, the main peak of the NCM811 exposed surface O 1s spectrum is located at ~531.7 eV, while a clear shoulder is observed towards lower BE (~531.2 eV).

Notably, for both NCM523 and NCM811 the relative intensities of the metal-oxide feature and the broad overlapped secondary features change substantially between the surface to the sub-surface spectra. This is especially pronounced for the

pristine samples indicating a thinner layer of surface species to be present compared to the exposed samples. Apart from the changes in relative intensities, the surface and sub-surface spectra of the samples exhibit somewhat similar line positions and shapes, except for the pristine NCM523 where the secondary phase peak position clearly changes from ~531.7 eV at the surface to 531.2 eV in the sub-surface. The position and relative intensity compared to the main transition metal oxide peak of this sub-surface secondary feature is consistent with that of the spontaneously forming defective oxide components discussed earlier and, apart from a minor amount of Li_2CO_3 (evident from the Li 1s and C 1s spectra), suggest that the original NCM523 is being probed.

The identification of the chemical state of first row transition metals by XPS analysis is difficult due to the complexity of their 2p spectra, which often feature asymmetric peaks, complex multiplet splitting, shake-up and plasmon loss structure and overlapping binding energies.⁵⁷ Furthermore, the transition metal oxides studied here (particularly Ni and Co) are susceptible to oxidation by the ion beam etching process and it may thus not be clear whether the observed differences in chemistry between the surface and sub-surface spectra occur spontaneously or due to the sample processing.

The Ni 2p spectra of both NCM523 and NCM811 exhibit the characteristic major $2p_{3/2}$ feature at ~854.5 eV and minor $2p_{1/2}$ feature at ~872.2 eV as well as their corresponding satellites (marked by asterisks). The high degree of overlap of the features along with the large number of candidate chemistries makes it difficult to accurately deconvolute the constituent peaks and assign related Ni chemical environments. The shape and position of the Ni 2p XPS signal from the surface of the pristine and exposed samples (both NCM523 and NCM811) are very similar indicating similar Ni chemistries to be present irrespective of NCM composition and exposure. However, a ~1.0-1.5 eV shift in the main $2p_{3/2}$ peak position is observed between the surface and corresponding sub-surface spectra suggesting a change in Ni chemical environment, *e.g.* the presence of $\text{Ni}(\text{OH})_2$, but as mentioned earlier could also be induced by the ion beam etching process.

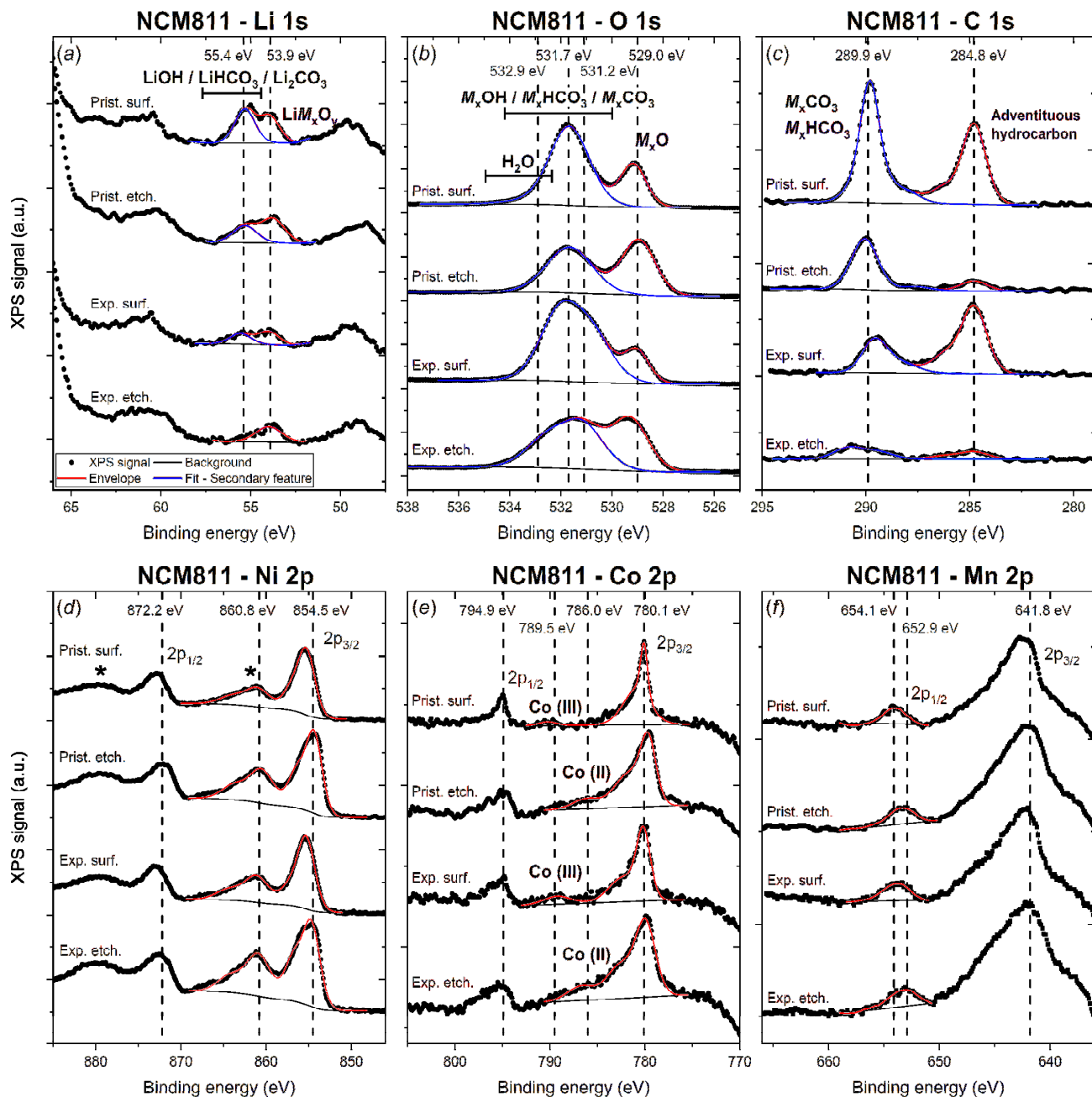


Figure 10: Stacked plots of background normalized XPS spectra of the a) Li 1s region, b) O 1s region, c) C 1s region, d) Ni 2p region, e) Co 2p region, and f) Mn 2p region of the pristine and D₂O liquid exposed (>2.5 years) NCM811 sample. For each sample spectra were collected from the as-received surface and after 300 s of ion beam etching to approximately 50 nm depth.

Similarly, the Co 2p spectra exhibit a main 2p_{3/2} feature at ~780.1 eV and a secondary 2p_{1/2} peak at ~794.9 eV. For both NCM523 and NCM811, the surface spectra show a relatively narrow 2p_{3/2} line with an associated satellite feature at approximately ~789.5 eV, while the sub-surface 2p_{3/2} lines have a broader shoulder towards higher BE along with a satellite at ~786.0 eV. The position of the main 2p_{3/2} peak does not change significantly between the surface and the sub-surface, however,

the observed change in line shape and satellite position indicates changes in chemistry and/or oxidation state.^{51, 58} The broad sub-surface Co 2p_{3/2} line shape and satellite at ~786.0 eV is characteristic for Co in the divalent state, *e.g.* in Co(OH)₂ or CoO, while the narrower peak shape with a satellite at ~789.5 eV in the surface spectra suggests that Co is oxidized.⁵⁷

Like Ni and Co, the Mn 2p spectra comprise a main 2p_{3/2} peak at ~641.8 eV and a secondary 2p_{1/2} peak at higher BE around 653 eV. Different Mn-oxide compounds, *e.g.* MnO, Mn₂O₃ and MnO₂, exhibit unique Mn 2p line features which can be used for identification.⁵⁷ Most notably, the spectrum of rock-salt MnO exhibits a characteristic shake-up satellite feature at ~646 eV. However, the Mn spectra of all present samples have very broad complex line shapes, which suggests several different Mn chemical environments to be present and prevents identification of the subtle characteristic features. For both NCM523 and NCM811, no clear difference is observed between the Mn 2p line shape of the pristine and exposed surface spectra or between the surface and sub-surface spectra. However, a clear BE shift in the Mn 2p line is observed between the surface and the etched spectra indicating a change in Mn-chemistry or oxidation state. This is particularly pronounced for the 2p_{1/2} peak which goes from ~654.1 eV at the surface to ~652.9 eV in the sub-surface.

The C 1s spectra generally exhibit two predominant features at BEs of ~284.8 eV and ~289.9 eV, which can be ascribed to adventitious hydrocarbon (C-C and C-H chemistry) and metal-carbonate (M_xCO_3) or metal-bicarbonate (M_xHCO_3) species, respectively. The presence of carbonate species even on the pristine sample is in agreement with the literature.^{13, 45} Notably, the C 1s spectra of the D₂O exposed surfaces of NCM523 and NCM811 show less C in carbonate species compared to the corresponding pristine surfaces. This could indicate that the long-term exposure of NCM523 and NCM811 powders to liquid water, and the associated secondary phases formed, inhibit/prevent formation of metal-carbonate surface species. Notably, Li₂CO₃ is soluble in water and the results could therefore also be consistent with surface Li₂CO₃ dissolving into the D₂O.

3.3.2. XPS - Quantitative analysis

Firstly, we note that conducting quantitative elemental and chemical analysis of XPS spectra is a highly complex task, in particular when it comes to quantifying different chemical environments. The number of implemented peaks, their respective positions/widths and the interpretation of their chemical meaning are often somewhat subjectively chosen, and care must be taken not to draw unjustified conclusions. Quantification on a relative scale and comparison of similar samples (consistent measurements and data treatment) are generally reliable but absolute values may have a great deal of uncertainty. This, along with the concerns and caveats discussed in the previous section, has therefore been taken into consideration in the present analysis. The employed background (black line), fitted envelopes (red line) and fit to secondary features of interest (blue line)

from the peak fitting of the respective XPS lines are shown in Figure 9 and Figure 10. The obtained elemental compositions of the samples are given in Table 3 and Figure 11, and the results of the quantitative elemental and chemical analyses of the obtained spectra are summarized in Table 4 and Figure 11. Further details regarding the peak fitting parameters of the different spectra may be found in the Supporting Information.

Table 3: Results of the quantitative elemental analysis of XPS spectra. The atomic percentages have been calculated from the fitted peak intensities corrected for the respective atomic sensitivity factors, electron mean free path, instrument transmission function and energy compensation factor.

Sample	Li (at. %)	Ni (at. %)	Co (at. %)	Mn (at. %)	O (at. %)	C (at. %)	Add. (at. %)
NCM523							
Pristine surface	15.09	6.67	2.63	3.25	55.76	15.14	1.46
Pristine etched	13.27	16.88	6.08	5.53	54.29	3.95	-
Exposed surface	4.58	10.00	2.91	3.94	68.78	9.64	0.15
Exposed etched	4.56	14.93	4.9	5.33	67.6	2.68	-
NCM811							
Pristine surface	17.15	10.38	1.21	0.79	54.26	15.4	0.81
Pristine etched	16.31	19.06	2.26	1.29	55.34	5.72	-
Exposed surface	8.14	13.31	1.70	1.08	65.48	10.01	0.27
Exposed etched	6.89	22.39	2.92	1.38	63.54	2.88	-

Note: Additional (Add.) comprises trace levels of other elements such as sulfur(adventitious) and indium (foil used for sample mounting).

For the NCM523 sample (surface and etched) a substantially higher Li-content is observed in the pristine (~13-15 at.%) compared to the exposed samples (~4.6 at.%). This difference is mainly due to the contribution from the secondary LiOH/LiHCO₃/Li₂CO₃ component (see Table 4), which constitutes ~56% of the total Li signal in both of the pristine spectra while being absent in the exposed samples. Similar behavior is seen for the NCM811 sample, where the pristine spectra show ~16-17 at.% Li while the exposed only show ~7-8 at.%. Of this Li signal, ~56% for the NCM811 pristine surface and ~42% for the NCM811 pristine sub-surface comes from secondary LiOH/LiHCO₃/Li₂CO₃ species, while it constitutes ~44% and 0% of the smaller amount of Li in the exposed NCM811 surface and sub-surface spectra, respectively. Interestingly, this indicates that the D₂O exposed NCM CAMs are either less-susceptible to formation of Li-containing surface species compared to the pristine compounds or that any formed Li₂CO₃ potentially dissolves in the D₂O. For the pristine NCM523 and NCM811 samples, a decrease in overall Li content (which is further enhanced considering the concurrent decrease in the amount of carbon) is observed in the sub-surface compared to the outer surface of the samples. Furthermore, the ratio between Li and the

transition metals in the sub-surface is considerably lower (*i.e.* $[\text{Li}]_{\text{total}}:[\text{Ni}+\text{Co}+\text{Mn}]_{\text{total}} = 0.5:1$ for pristine NCM523 and 0.7:1 for pristine NCM811) than the expected 1:1 ratio of the NCM parent material. This Li-deficiency could indicate the presence of spinel (*e.g.* LiNi_2O_4) and/or rock-salt (*e.g.* NiO) phases in the sub-surface region due Li-depletion induced by the formation of Li-rich surface species ($\text{LiOH}/\text{LiHCO}_3/\text{Li}_2\text{CO}_3$). It should be noted that XPS has a relatively low sensitivity to Li and the obtained absolute atomic percentages of Li from the spectra may thus be the least accurate value of the constituent elements, but the relative changes discussed here are consistent and clear.

A substantially higher oxygen content (both surface and sub-surface) is observed for the exposed compared to the pristine samples (~13 at.% higher for NCM523 and ~8-11 at.% higher for NCM811), which could indicate the presence of adsorbed surface water. However, little-to-no difference in oxygen content is observed between the surface and corresponding etched spectra of each sample. The distribution of oxygen chemical environment (additional phases and oxide-lattice) varies substantially both between pristine and exposed, as well as between surface and sub-surface (see Table 4 and Figure 11). For NCM523, the surface of the pristine and D_2O exposed samples exhibit very similar percentage of “lattice oxygen” (~21-23% of total O), while a substantially higher degree of lattice oxygen is seen in the sub-surface of the pristine (~59.9% of total O) compared to exposed (~40.5% of total O). Similar results are obtained from the NCM811 spectra with lattice oxygen constituting ~25.5% of the total oxygen at the pristine surface and ~14.4% in the exposed surface, while making up ~46.5% in the pristine sub-surface and ~37.7% in the exposed sub-surface. The observed variations indicate a thicker surface layer to be present in the exposed compared to the pristine samples. Due to the complexity of the O 1s feature in the ~530-534 eV BE-range (discussed in the previous section), which contains the contributions from secondary $M_x\text{CO}_3$, $M_x\text{OH}$, H_2O , *etc.*, attempting to deconvolute its features and extract reliable quantitative chemical information was deemed unfeasible.

Table 4: Results of the quantitative chemical analysis of the Li 1s, O 1s and C 1s XPS spectra. The atomic percentages have been calculated from the fitted peak intensities corrected for the respective atomic sensitivity factors, electron mean free path, instrument transmission function and energy compensation factor.

Sample	Lithium		Transition metals	Oxygen		Carbon	
	Li oxide (at. %)	LiOH/LiHCO ₃ /Li ₂ CO ₃ (at. %)	[Ni+Co+Mn] (at. %)	M _x O (at. %)	M _x OH/M _x CO ₃ /H ₂ O (at. %)	M _x CO ₃ (at. %)	Adv. (at. %)
NCM523							
Pristine surface	6.58	8.51	12.55	11.95	43.81	6.90	8.24
Pristine etched	5.87	7.40	28.49	32.50	21.79	3.24	0.71
Exposed surface	4.58	-	16.85	15.61	53.17	1.28	8.36
Exposed etched	4.56	-	25.16	27.4	40.20	0.50	2.18
NCM811							
Pristine surface	7.47	9.68	12.38	13.83	40.43	8.77	6.63
Pristine etched	9.49	6.82	22.61	25.73	29.61	4.85	0.87
Exposed surface	4.53	3.61	16.09	9.46	56.02	3.38	6.63
Exposed etched	6.89	-	26.69	23.98	39.56	1.84	1.04

As evident from the intensity differences in the C 1s spectra in Figure 9 and Figure 10, the pristine surfaces of NCM523 and NCM811 clearly exhibit a larger amount of $M_x\text{HCO}_3/M_x\text{CO}_3$ species (6.90 at.% and 8.77 at.%) compared to their D₂O exposed counterparts (1.28 at.% and 3.38 at.%). The seemingly correlated change in the amount of secondary Li-containing phases in the Li 1s spectra (discussed above) suggests that Li₂CO₃ and/or LiHCO₃ species are present in the pristine surface, while the long-term D₂O exposure of the samples seemingly prevents the formation of carbonate species. Following ion beam etching, the amount of carbonate and adventitious carbon drops substantially for all samples confirming that they are part of a thin outer layer of secondary surface phases formed due to ambient exposure rather than bulk impurities, *e.g.* from homogeneous CAM degradation or residual synthesis precursors. For the NCM523 pristine sample, the ratio between the amount Li in LiOH/LiHCO₃/Li₂CO₃ determined from the Li 1s peak fitting and the amount of C in $M_x\text{CO}_3$ obtained from the C 1s analysis (assuming no transition metal carbonates to be formed) is ~1:1 at the surface (indicative of LiHCO₃) and increases up to ~2:1 (indicative of Li₂CO₃) in the sub-surface. The same trend, but less pronounced, is observed for NCM811 pristine. Notably, for all samples the amount of oxygen in $M_x\text{CO}_3$ chemistry, inferred from the amount of carbon in $M_x\text{CO}_3$, does not account for the amount of oxygen in secondary (non-metal oxide) phases obtained from the fitting of the O 1s spectrum. This

indicates that, apart from the parent NCM material and $\text{LiHCO}_3/\text{Li}_2\text{CO}_3$, a substantial amount of additional oxygen containing species, such as H_2O (adsorbed/lattice) or transition metal hydroxides ($\text{Ni}(\text{OH})_2$, $\text{Co}(\text{OH})_2$, $\text{Mn}(\text{OH})_2$), are present.

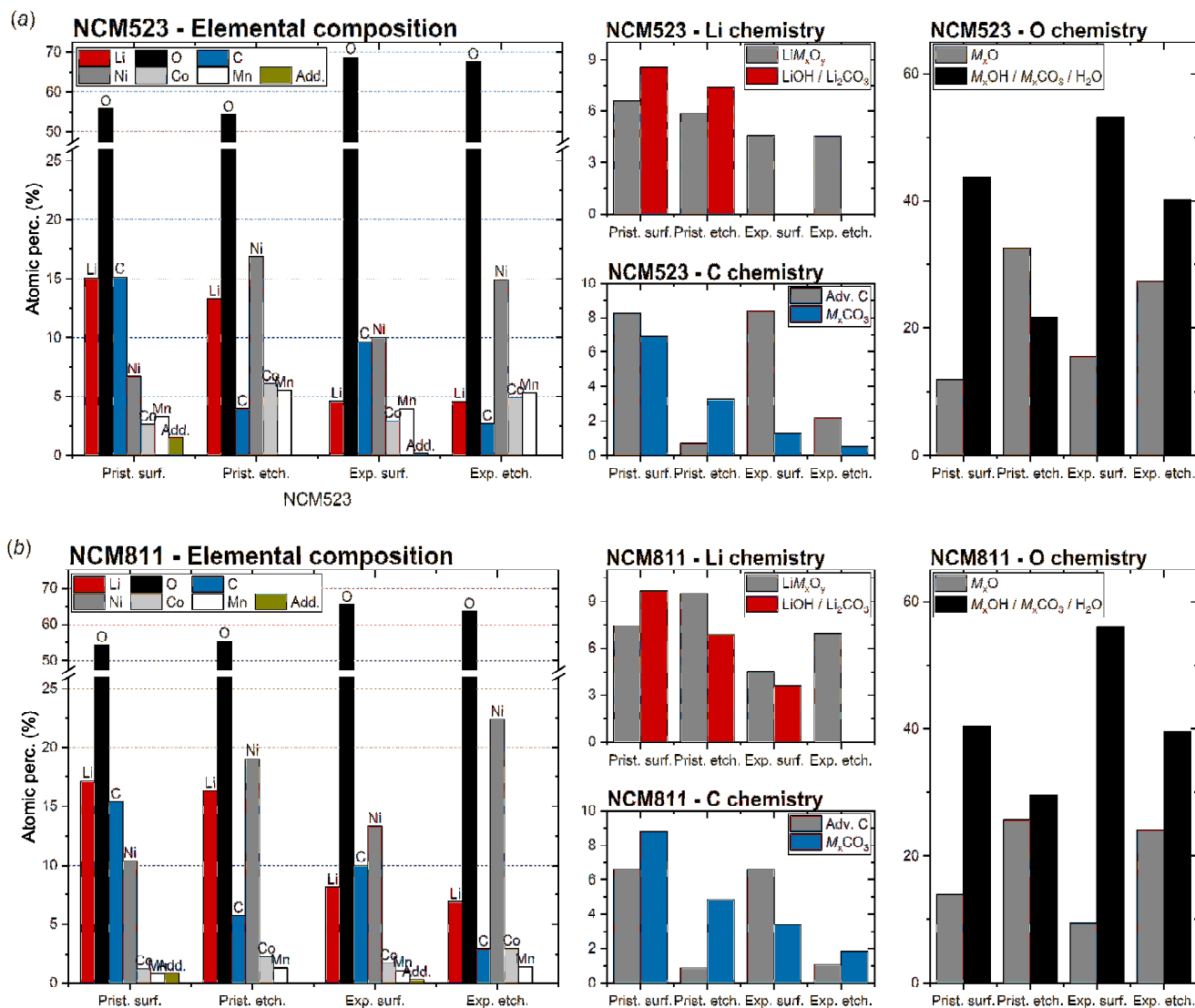


Figure 11: Bar plots of the results from the quantitative elemental (left) and chemical (right) analysis of the XPS spectra from a) NCM523 and b) NCM811 illustrating the relative differences in composition and chemistry of the samples.

As discussed earlier, the peak fitting of the transition metal spectra did not allow reliable quantitative chemical information to be extracted. For both NCM523 and NCM811, a slightly higher absolute concentration of all transition metals (despite the significantly higher oxygen content) is observed in the exposed compared to the pristine surfaces (see Table 3 and Figure 11), which is consistent with an outer layer of $\text{LiHCO}_3/\text{Li}_2\text{CO}_3$ being present in the pristine and not in the exposed samples.

Considering the lower Li content and the observed variations in oxygen chemistries (discussed earlier), the higher transition metal content is consistent with presence of transition metal hydroxide species. In all samples, the concentrations of all transition metals (Ni, Co and Mn) increase substantially after ion beam etching due to the removal of surface impurities such as adsorbed water, adventitious organics, *etc.* For all samples, the transition metal concentration with respect to the amount of Li in the NCM chemistry is found to be higher than expected for the parent materials ($\text{LiNi}_{0.5}\text{Co}_{0.2}\text{Mn}_{0.3}\text{O}_2$ and $\text{LiNi}_{0.8}\text{Co}_{0.1}\text{Mn}_{0.1}\text{O}_2$) (see Table 4). This again indicates the presence of Li-depleted/free phases such as transition metal hydroxides ($\text{Ni}(\text{OH})_2$, $\text{Co}(\text{OH})_2$, $\text{Mn}(\text{OH})_2$) or spinel (*e.g.* LiNi_2O_4) and/or rock-salt (*e.g.* NiO) metal oxides. For both pristine and exposed as well as the surface and sub-surface NCM523 and NCM811 samples, the relative ratio between the transition metals (Ni:Co:Mn) from the elemental analysis remain close to the expected nominal 5:2:3 and 8:1:1 ratios of the compounds, with a slightly low Mn-content generally being observed (see Figure 11). In a recent study by Bichon *et al.* a partial Mn-depletion in the surface region of NCM particles was also observed by EELS elemental mapping.¹⁹

3.3.3. Possible surface/sub-surface composition

The spectral features and surface composition/chemistry observed here are generally in agreement with previous reports in the literature. Differences can generally be attributed to electrode components and variations in exposure type, thermal treatment, electrochemical cycling, *etc.* The NCM CAM surface composition and chemistry examined here are clearly complex and many caveats exists in the both the qualitative, but especially quantitative, analyses of the XPS spectra. However, based on the relative changes in the spectra as a result of D_2O exposure and/or ion beam-etching discussed above, we propose the following simplified surface composition/structure (see Figure 12).

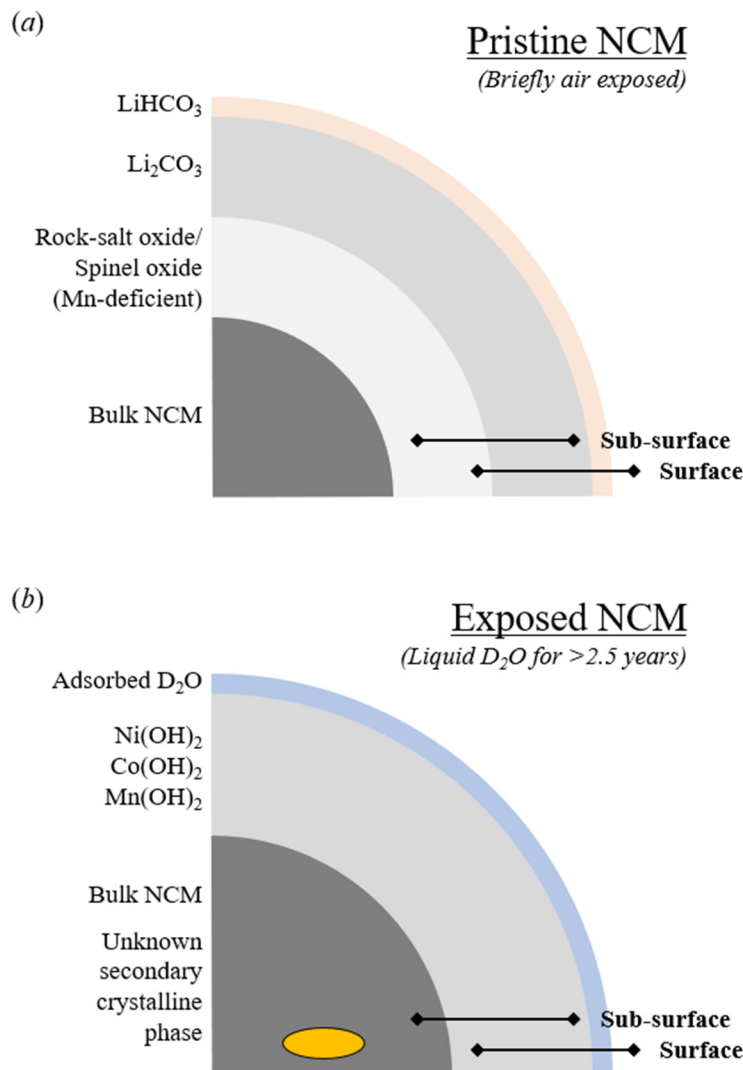


Figure 12: Simplified illustration of the proposed surface (<10 nm) and sub-surface (~ 50 nm) compositions of the a) pristine NCM samples and b) D_2O liquid exposed NCM samples based on the qualitative analysis of XPS spectra.

In summary, the present XPS data suggests that a thin $\text{LiHCO}_3/\text{Li}_2\text{CO}_3$ outer layer forms on the surface of the pristine NCM523 and NCM811 samples (likely as a result of brief exposure to ambient air during XPS sample preparation). The extraction of Li needed to form these surface species leads to formation of sub-surface region containing Li-deficient transition metal oxides, such as spinel (*e.g.* LiNi_2O_4) and/or rock-salt (*e.g.* NiO) phases. The D_2O exposed samples, on the other hand, do not exhibit formation any significant amount of carbonate species but rather show evidence of an outer layer of adsorbed D_2O and an underlying layer of transition metal hydroxides along with the parent NCM phase. The XPS analysis did not unveil any new clues as to the identity of the unknown crystalline secondary phase found in the NPD data. We also note that the

amounts of the various surface phases observed by XPS are either too small to be observed in the NPD data or the compounds are “powder diffraction amorphous”.

4. Conclusion

The long-term stability of two different Ni-rich layered transition metal oxide compounds, namely $\text{Li}_x\text{Ni}_{0.5}\text{Co}_{0.2}\text{Mn}_{0.3}\text{O}_2$ and $\text{Li}_x\text{Ni}_{0.8}\text{Co}_{0.1}\text{Mn}_{0.1}\text{O}_2$, exposed to deuterated water (vapor and liquid) for a period of >2.5 years have been studied using neutron powder diffraction. Structural modelling of NPD data allows true representative bulk-level structural information to be extracted in contrast to surface-limited techniques such as XPS or electron microscopy. The data reveals the formation of a secondary phase which does not match any previously reported exposure products for this system and could not be identified. This unknown secondary phase appears in all exposed samples but forms faster in the liquid- compared to the vapor-exposed compounds. Interestingly, the formation of the secondary phase does not induce any observable structural changes in the NCM523 and NCM811 parent phases. Thus, the present NPD data analysis implies that the secondary phase is formed by the transformation of the parent phase rather than its modification. The NCM523 and NCM811 compounds exhibit ~4% and ~0% Li/Ni anti-site defect concentrations, respectively, which remain consistent irrespective of exposure type and duration. Furthermore, no proton-lithium exchange trend is detectable by neutron diffraction in the sample bulk as a result of the water exposure. The bulk NPD characterization is complemented by analysis of the surface composition and chemistry of the pristine and long-term liquid D_2O exposed samples by XPS. The spectra indicate formation of a thin $\text{LiHCO}_3/\text{Li}_2\text{CO}_3$ outer layer at the surface of the pristine (briefly air exposed) NCM523 and NCM811 compounds along with a Li-deficient oxide phase in the sub-surface region. The XPS data on long-term D_2O liquid exposed samples show little-to-no carbonate species but instead show evidence of adsorbed water and a thicker transition metal hydroxide layer.

Acknowledgements

The oxide powders used in this work are from Argonne’s Cell Analysis, Modeling and Prototyping (CAMP) Facility, which is supported with core funding from the Applied Battery Research (ABR) for Transportation Program. We are grateful to Bryant Polzin for providing the oxides. The authors acknowledge use of facilities and the assistance of Dr. Bill Gong and Songyan Yin in the Solid State & Elemental Analysis Unit at Mark Wainwright Analytical Centre.

Funding information

This work was supported by the Carlsberg Foundation (grant no. CF18-0519 and CF19-0143), Australian Research Council Discovery programs (DP170100269 and DP200100959) and Research Training Program and the Australian Institute of Nuclear Science and Engineering (AINSE) postgraduate research award scheme.

References

1. N. Nitta, F. X. Wu, J. T. Lee and G. Yushin, *Mater. Today*, 2015, **18**, 252-264.
2. D. Larcher and J. M. Tarascon, *Nat. Chem.*, 2015, **7**, 19-29.
3. D. Andre, S. J. Kim, P. Lamp, S. F. Lux, F. Maglia, O. Paschos and B. Stiaszny, *J. Mater. Chem. A*, 2015, **3**, 6709-6732.
4. G. E. Blomgren, *J. Electrochem. Soc.*, 2017, **164**, A5019-A5025.
5. J. Kim, H. Lee, H. Cha, M. Yoon, M. Park and J. Cho, *Adv. Energy Mater.*, 2018, **8**, 1702028.
6. K. Mizushima, P. C. Jones, P. J. Wiseman and J. B. Goodenough, *Mater. Res. Bull.*, 1980, **15**, 783-789.
7. M. D. Radin, S. Hy, M. Sina, C. C. Fang, H. D. Liu, J. Vinckeviciute, M. H. Zhang, M. S. Whittingham, Y. S. Meng and A. Van der Ven, *Adv. Energy Mater.*, 2017, **7**, 1602888.
8. M. H. Kim, H. S. Shin, D. Shin and Y. K. Sun, *J. Power Sources*, 2006, **159**, 1328-1333.
9. E. M. Erickson, F. Schipper, T. R. Penki, J. Y. Shin, C. Erk, F. F. Chesneau, B. Markovsky and D. Aurbach, *J. Electrochem. Soc.*, 2017, **164**, A6341-A6348.
10. A. Manthiram, J. C. Knight, S. T. Myung, S. M. Oh and Y. K. Sun, *Adv. Energy Mater.*, 2016, **6**, 1501010.
11. W. Liu, P. Oh, X. Liu, M. J. Lee, W. Cho, S. Chae, Y. Kim and J. Cho, *Angew. Chem. Int. Ed.*, 2015, **54**, 4440-4457.
12. I. A. Shkrob, J. A. Gilbert, P. J. Phillips, R. Klie, R. T. Haasch, J. Bareno and D. P. Abraham, *J. Electrochem. Soc.*, 2017, **164**, A1489-A1498.
13. R. Jung, R. Morasch, P. Karayaylali, K. Phillips, F. Maglia, C. Stinner, Y. Shao-Horn and H. A. Gasteiger, *J. Electrochem. Soc.*, 2018, **165**, A132-A141.
14. J. Sicklinger, M. Metzger, H. Beyer, D. Pritzl and H. A. Gasteiger, *J. Electrochem. Soc.*, 2019, **166**, A2322-A2335.
15. Z. Q. Chen, J. Wang, J. X. Huang, T. Fu, G. Y. Sun, S. B. Lai, R. Zhou, K. Li and J. B. Zhao, *J. Power Sources*, 2017, **363**, 168-176.
16. N. V. Faenza, L. Bruce, Z. W. Lebens-Higgins, I. Plitz, N. Pereira, L. F. J. Piper and G. G. Amatucci, *J. Electrochem. Soc.*, 2017, **164**, A3727-A3741.
17. K. Matsumoto, R. Kuzuo, K. Takeya and A. Yamanaka, *J. Power Sources*, 1999, **81**, 558-561.
18. K. Shizuka, C. Kiyohara, K. Shima and Y. Takeda, *J. Power Sources*, 2007, **166**, 233-238.
19. M. Bichon, D. Sotta, N. Dupré, E. De Vito, A. Boulineau, W. Porcher and B. Lestriez, *ACS Applied Materials & Interfaces*, 2019, **11**, 18331-18341.
20. N. Alias and A. A. Mohamad, *J. Power Sources*, 2015, **274**, 237-251.
21. D. Pritzl, T. Teufl, A. T. S. Freiberg, B. Strehle, J. Sicklinger, H. Sommer, P. Hartmann and H. A. Gasteiger, *J. Electrochem. Soc.*, 2019, **166**, A4056-A4066.
22. Y. Shi, M. H. Zhang, C. C. Fang and Y. S. Meng, *J. Power Sources*, 2018, **394**, 114-121.
23. K. Momma and F. Izumi, *J. Appl. Crystallogr.*, 2011, **44**, 1272-1276.
24. H. S. Liu, Z. R. Zhang, Z. L. Gong and Y. Yang, *Electrochem Solid St.*, 2004, **7**, A190-A193.
25. X. B. Zheng, X. H. Li, Z. X. Wang, H. J. Guo, Z. J. Huang, G. C. Yan and D. Wang, *Electrochim. Acta*, 2016, **191**, 832-840.
26. L. Yin, Z. Li, G. S. Mattei, J. Zheng, W. Zhao, F. Omenya, C. Fang, W. Li, J. Li, Q. Xie, E. M. Erickson, J.-G. Zhang, M. S. Whittingham, Y. S. Meng, A. Manthiram and P. G. Khalifah, *Chem. Mater.*, 2019, DOI: 10.1021/acs.chemmater.9b03646.
27. K. D. Liss, B. Hunter, M. Hagen, T. Noakes and S. Kennedy, *Physica B*, 2006, **385-86**, 1010-1012.
28. M. Avdeev and J. R. Hester, *J. Appl. Crystallogr.*, 2018, **51**, 1597-1604.
29. J. Rodriguez-Carvajal, *Physica B Condens. Matter*, 1993, **192**, 55-69.
30. P. Thompson, D. E. Cox and J. B. Hastings, *J. Appl. Crystallogr.*, 1987, **20**, 79-83.
31. K. Marker, P. J. Reeves, C. Xu, K. J. Griffith and C. P. Grey, *Chem. Mater.*, 2019, **31**, 2545-2554.

32. V. Valvoda, *International Tables for Crystallography, Volume C: Mathematical, Physical and Chemical Tables, Chapter 4*, Kluwer Academic Publishers, Dordrecht/Boston/London, 3 edn., 2004.
33. X. H. Xiong, Z. X. Wang, P. Yue, H. J. Guo, F. X. Wu, J. X. Wang and X. H. Li, *J. Power Sources*, 2013, **222**, 318-325.
34. T. Degen, M. Sadki, E. Bron, U. Konig and G. Nenert, *Powder Diff.*, 2014, **29**, S13-S18.
35. A. Altomare, C. Cuocci, C. Giacovazzo, A. Moliterni, R. Rizzi, N. Corriero and A. Falcicchio, *J. Appl. Crystallogr.*, 2013, **46**, 1231-1235.
36. Y. Idemoto, J. W. Richardson, N. Koura, S. Kohara and C. K. Loong, *J. Phys. Chem. Solids*, 1998, **59**, 363-376.
37. S. Mair, *Acta Crystallogr., Sect. A: Found. Adv.*, 1978, **34**, 542-547.
38. F. Pertlik, *Acta Crystallogr. C*, 1986, **42**, 4-5.
39. G. Dutta, A. Manthiram, J. B. Goodenough and J. C. Grenier, *J. Solid State Chem.*, 1992, **96**, 123-131.
40. S. Sasaki, K. Fujino and Y. Takeuchi, *P. Jpn. Acad. B-Phys.*, 1979, **55**, 43-48.
41. W. S. Yoon, K. Y. Chung, J. McBreen and X. Q. Yang, *Electrochem. Comm.*, 2006, **8**, 1257-1262.
42. C. Ghanty, B. Markovsky, E. M. Erickson, M. Talianker, O. Haik, Y. Tal-Yossef, A. Mor, D. Aurbach, J. Lampert, A. Volkov, J. Y. Shin, A. Garsuch, F. F. Chesneau and C. Erk, *ChemElectroChem*, 2015, **2**, 1479-1486.
43. M. L. Foo, T. Klimczuk and R. J. Cava, *Mater. Res. Bull.*, 2005, **40**, 665-670.
44. X. Zhang, W. J. Jiang, X. P. Zhu, A. Mauger, Qilu and C. M. Julien, *J. Power Sources*, 2011, **196**, 5102-5108.
45. H. S. Liu, Y. Yang and J. J. Zhang, *J. Power Sources*, 2006, **162**, 644-650.
46. J. Eom, M. G. Kim and J. Cho, *J. Electrochem. Soc.*, 2008, **155**, A239.
47. G. V. Zhuang, G. Y. Chen, J. Shim, X. Y. Song, P. N. Ross and T. J. Richardson, *J. Power Sources*, 2004, **134**, 293-297.
48. Y. Zhao, S. Wang, W. Ren and R. Wu, *J. Electrochem. Soc.*, 2012, **160**, A82-A86.
49. R. Moshtev, P. Zlatilova, S. Vasilev, I. Bakalova and A. Kozawa, *J. Power Sources*, 1999, **81-82**, 434-441.
50. D.-H. Cho, C.-H. Jo, W. Cho, Y.-J. Kim, H. Yashiro, Y.-K. Sun and S.-T. Myung, *J. Electrochem. Soc.*, 2014, **161**, A920-A926.
51. J. F. Moulder and J. Chastain, *Handbook of X-ray Photoelectron Spectroscopy: A Reference Book of Standard Spectra for Identification and Interpretation of XPS Data*, Physical Electronics Division, Perkin-Elmer Corporation, 1992.
52. R. T. Haasch, S. E. Trask and D. P. Abraham, *Surface Science Spectra*, 2019, **26**, 014002.
53. Z. Fu, J. Hu, W. Hu, S. Yang and Y. Luo, *Applied Surface Science*, 2018, **441**, 1048-1056.
54. R. T. Haasch and D. P. Abraham, *Surface Science Spectra*, 2019, **26**, 014006.
55. R. T. Haasch and D. P. Abraham, *Surface Science Spectra*, 2019, **26**, 014004.
56. M. C. Biesinger, B. P. Payne, L. W. M. Lau, A. Gerson and R. S. C. Smart, *Surface and Interface Analysis*, 2009, **41**, 324-332.
57. M. C. Biesinger, B. P. Payne, A. P. Grosvenor, L. W. M. Lau, A. R. Gerson and R. S. C. Smart, *Applied Surface Science*, 2011, **257**, 2717-2730.
58. N. Weidler, S. Paulus, J. Schuch, J. Klett, S. Hoch, P. Stenner, A. Maljusch, J. Brötz, C. Wittich, B. Kaiser and W. Jaegermann, *Phys. Chem. Chem. Phys.*, 2016, **18**, 10708-10718.
59. N. Weidler, J. Schuch, F. Knaus, P. Stenner, S. Hoch, A. Maljusch, R. Schäfer, B. Kaiser and W. Jaegermann, *J. Phys. Chem. C*, 2017, **121**, 6455-6463.